PHYSICS

Layer-engineered interlayer excitons

Qinghai Tan[1], Abdullah Rasmita[1], Si Li[2,3], Sheng Liu[1], Zumeng Huang[1], Qihua Xiong[4], Shengyuan A. Yang[2]*, K. S. Novoselov[5]*, Wei-bo Gao[1,6]*

Photoluminescence (PL) from excitons serves as a powerful tool to characterize the optoelectronic property and band structure of semiconductors, especially for atomically thin two-dimensional transition metal dichalcogenide (TMD) materials. However, PL quenches quickly when the thickness of TMD materials increases from monolayer to a few layers, due to the change from direct to indirect band transition. Here, we show that PL can be recovered by engineering multilayer heterostructures, with the band transition reserved to be a direct type. We report emission from layer-engineered interlayer excitons from these multilayer heterostructures. Moreover, as desired for valleytronics devices, the lifetime, valley polarization, and valley lifetime of the generated interlayer excitons can all be substantially improved as compared with that in the monolayer-monolayer heterostructure. Our results pave the way for controlling the properties of interlayer excitons by layer engineering.

INTRODUCTION

Layered transition metal dichalcogenides (TMDs) MX_2 (M = W and Mo, and X = S and Se) provide a platform for fundamental research and optoelectronic devices using an atomically thin material (*1*). For optoelectronic applications, to have efficient light emission, a semiconductor with a direct bandgap nature is required (*2*–*4*). However, bilayer or multilayer MX_2 has an indirect bandgap, quenching its light emission to a large extent (*2*, *5*). In this work, we show that van der Waals (vdW) heterostructures (*6*) formed by the stacking of two different MX_2 can convert an indirect bandgap material to a direct type and therefore recover its photoluminescence (PL) emission.

In particular, the light emission of interlayer excitons (IXs) (*7*–*9*) in our monolayer (1L) WSe_2/few-layer (mL) MoS_2 heterostructures shows fascinating valley properties (*7*–*9*), where the lifetimes, valley polarization, and valley relaxation lifetimes improve remarkably. Valley, defined as local band extreme in momentum space, represents one potential degree of freedom to carry and process information (*10*–*12*) in valley spintronics. Therein, a long valley lifetime and high valley degree of polarization (DOP) is desired. However, the picosecond time scale depolarization process of the intralayer excitons in the monolayer TMDs markedly limits its application (*13*, *14*). For the IXs in the bilayer heterostructures, the electrons and holes are separated in different layers, thus reducing the electron-hole exchange interaction. This spatially indirect nature of the IXs results in their high valley polarization and long lifetime (*7*, *9*, *15*–*17*), which brings promising opportunities for high-temperature exciton condensation (*17*, *18*) and valley physics (*7*, *9*, *15*–*17*, *19*–*22*). Different knobs have been shown to be effective ways to tune the properties of IXs, for instance, the twist angles (*19*, *23*–*27*). The IXs formed in a bilayer heterostructure with small twist angles lead to the Moiré physics (*19*, *25*–*27*).

In this study, we show that, in addition to controlling the stacking angle in a bilayer heterostructure system, varying the number of layers provides another natural degree of freedom to modulate the vdW heterostructure properties. Two types of heterostructures are analyzed with different layer-dependent behaviors: mL-WSe_2/1L-MoS_2 and 1L-WSe_2/mL-MoS_2. For 1L-WSe_2/mL-MoS_2, the increase of layer numbers reduces the electron and hole cloud overlap, further increasing the valley lifetime of excitons, while the valley polarization almost vanishes for mL-WSe_2/1L-MoS_2 cases. In addition, we found that, for 1L-WSe_2/mL-MoS_2, a tiny magnetic field can suppress the valley relaxation and increase the valley lifetime from tens of nanoseconds by two orders to several microseconds. The suppression of valley relaxation has been directly observed from the time-resolved PL emission due to the slow valley relaxation in these multilayer vdW heterostructures. In the end, a more robust valley polarization can be sustained until room temperature in these multilayer heterostructures.

RESULTS AND DISCUSSION

IX spectrum

Figure 1 shows the microscopic image and the PL spectrum for different WSe_2/MoS_2 heterostructure samples. Figure 1 (A and B) shows the schematic of a multilayer heterostructure formed by different layers of MoS_2 and WSe_2. The electrons and holes are separated into the MoS_2 layer and the WSe_2 layers, respectively, forming the IXs (see inset in Fig. 1A). Figure 1C shows a typical optical image for the mL (here, m = 1 to 4) WSe_2/1L-MoS_2 sample, and Fig. 1D shows the image for 1L-WSe_2/mL-MoS_2 samples. The two-dimensional (2D) layers are first exfoliated mechanically from bulk crystals on polydimethylsiloxane (PDMS) stamps and then transferred to form the heterostructure by a dry transfer method. The details for sample preparation can be found in the methods section. We used second harmonic generation (SHG) to check the alignment to be AA stacking (section S1 and fig. S1) and Raman spectroscopy to characterize the sample quality, layer numbers, and interlayer coupling strength of the heterostructures (section S2 and figs. S2 and S3).

IX emission and intralayer exciton emission spectrum are shown in Fig. 1E. We note that the IX emission from the heterostructure lies in the infrared range, which is far away from the visible range of all intralayer exciton emission from WSe_2 and MoS_2. Thus, a pure

[1]Division of Physics and Applied Physics, School of Physical and Mathematical Sciences, Nanyang Technological University, Singapore 637371, Singapore. [2]Research Laboratory for Quantum Materials in Singapore University of Technology and Design, Singapore 487372, Singapore. [3]School of Physics, Northwest University, Xi' an 710069, China. [4]State Key Laboratory of Low-Dimensional Quantum Physics and Department of Physics, Tsinghua University, Beijing, China. [5]Department of Materials Science and Engineering, National University of Singapore, 9 Engineering Drive 1, Singapore 117575, Singapore. [6]The Photonics Institute and Centre for Disruptive Photonic Technologies, Nanyang Technological University, Singapore 637371, Singapore.
*Corresponding author. Email: shengyuan_yang@sutd.edu.sg (S.A.Y.); kostya@nus.edu.sg (K.S.N.); wbgao@ntu.edu.sg (W.-b.G.)

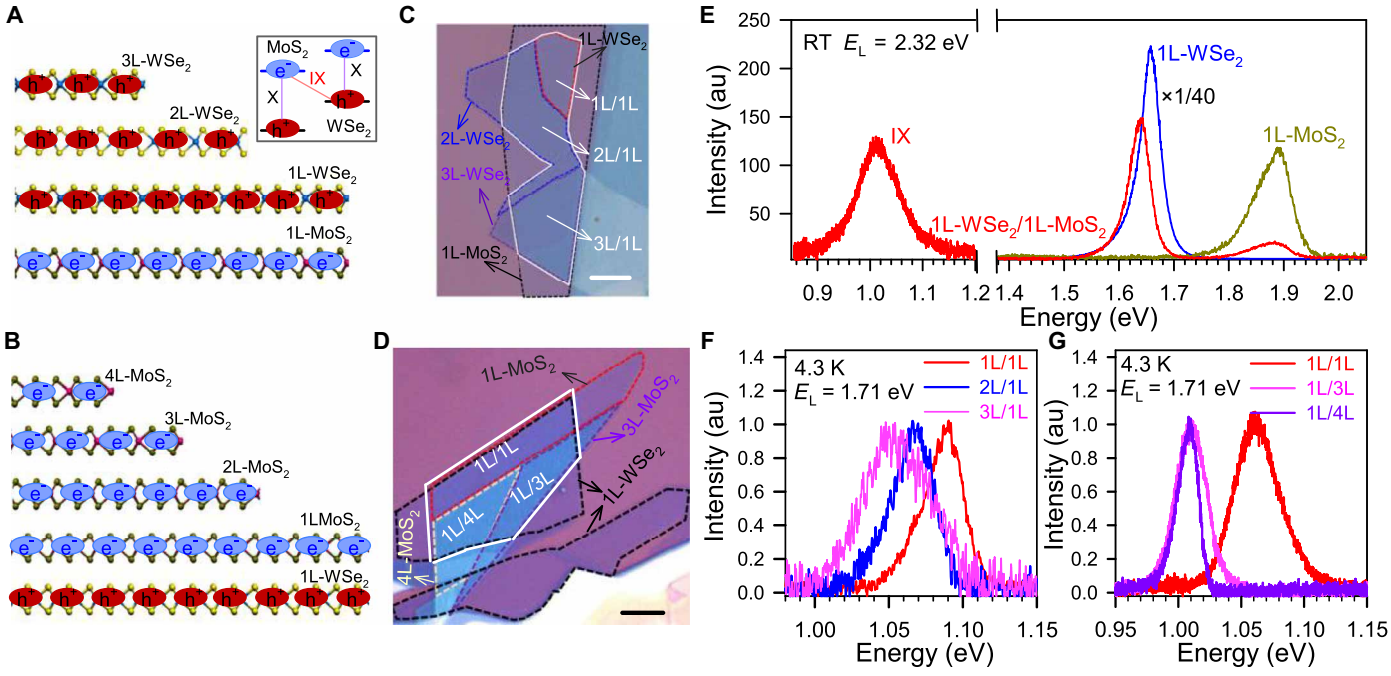

Fig. 1. Observation of IXs in mL-WSe_2/1L-MoS_2 and 1L-WSe_2/mL-MoS_2 heterostructures. (**A** and **B**) A schematic of the IXs in mL-WSe_2/1L-MoS_2 and 1L-WSe_2/mL-MoS_2 heterostructures (HS), respectively. The inset shows a type II band alignment of WSe_2/MoS_2 heterostructure [intralayer exciton (X); interlayer exciton (IX)]. For IX, the electrons and holes are separated in MoS_2 and WSe_2 layers, respectively. (**C** and **D**) The optical microscope image of the mL-WSe_2/1L MoS_2 (labeled as mL/1L; $m = 1$ to 3) sample (S1) and 1L-WSe_2/mL-MoS_2 (labeled as 1L/mL; $m = 1$, 3, and 4) sample (S2). WSe_2 and MoS_2 with different layers are marked with dashed lines of different colors. The heterostructure regions are marked with solid white lines. Scale bars, 10 μm. (**E**) The PL spectra of intralayer excitons in monolayer WSe_2 and MoS_2 and IXs in 1L-WSe_2/1L-MoS_2 heterostructure sample at room temperature (RT). (**F** and **G**) The PL spectra of IXs in mL-WSe_2/1L-MoS_2 heterostructure and 1L-WSe_2/mL-MoS_2 heterostructure at low temperature. au, arbitrary units.

IX signal can be obtained by using long-pass filters (e.g., a 1064-nm long pass). Figure 1 (F and G) shows the low-temperature PL spectra of IXs from the mL-WSe_2/1L-MoS_2 heterostructure (sample in Fig. 1C) and 1L-WSe_2/mL-MoS_2 heterostructure (sample in Fig. 1D). We can see that clear IX PL has been observed for all the samples with different spectrum shifts. When the number of WSe_2 (MoS_2) layers is increased, the IX PL spectra show a redshift up to 50 meV relative to that in the 1L/1L heterostructure case. We prepared several other heterostructure samples, with and without hexagonal Boron Nitride (hBN) encapsulation, and observed similar results (more sample images and characterizations are presented in section S3 and figs. S4 to S10). This redshift can be understood as a consequence of the increase in the effective dielectric constant with increasing number of layer (*28*). Also, we anticipate that this redshift is mainly due to the shifts of valence band of mL-WSe_2 and conduction band of mL-MoS_2, as well as the changes of IX binding energy in multilayer heterostructures (*29*). This makes IX energy highly tunable with the bandgap engineering (*30*). More results and discussions related to this PL redshift in multilayer heterostructure are shown in section S4 and figs. S11 and S12 in that section.

Temperature dependence of IX PL intensity

To understand more about the nature of the IX transition and band structure of the stacked heterostructure, we investigate the temperature dependence of PL emissions. Figure 2 (A and B) shows the PL intensity mapping of IXs in mL-WSe_2/1L-MoS_2 heterostructure at 4.3 K and room temperature, respectively. Here, the intralayer exciton emission is blocked by a 1064-nm long-pass filter, and therefore, only IX emission is relevant in the PL mapping. The intensity change as a function of temperature is shown in Fig. 2C. For both 1L-WSe_2/1L-MoS_2 and 2L-WSe_2/1L-MoS_2 cases, PL intensity decreases as the temperature increases (also see section S5 and figs. S13 to S15). This PL temperature dependence is consistent with the case of monolayer MoS_2 intralayer exciton (*31*) and IXs in 1L-WSe_2/1L-MoS_2 heterostructure (*8*) and can be understood by considering the reduced momentum mismatch between the band extrema and the increased radiative transition probability with decreased temperatures (*8*, *31*, *32*).

In contrast to the 1L-WSe_2/1L-MoS_2 and 2L-WSe_2/1L-MoS_2 case, when the number of WSe_2 layers is more than two in mL/1L heterostructure (e.g., $m = 3$), the PL intensity of the IXs tends to increase with increasing temperature (Fig. 2C). Similar results are observed in other samples (see section S5 and figs. S13 and S14). This indicates that the 3L-WSe_2/1L-MoS_2 heterostructure can be a momentum indirect bandgap semiconductor. This comes from the fact that the valence band maximum from multilayer WSe_2 changes from K to Γ point when the number of layers is increased to three. In this case, the indirect K-Γ transition is in the ground state, while the direct K-K transition has higher energy than the indirect K-Γ transition. Therefore, the PL emission intensity will increase with a higher temperature. We note that these results are consistent with the recent direct measurement of the valence band of 1L-3L WSe_2 by the micrometer-scale angle-resolved photoemission spectroscopy (microARPES) (*33*).

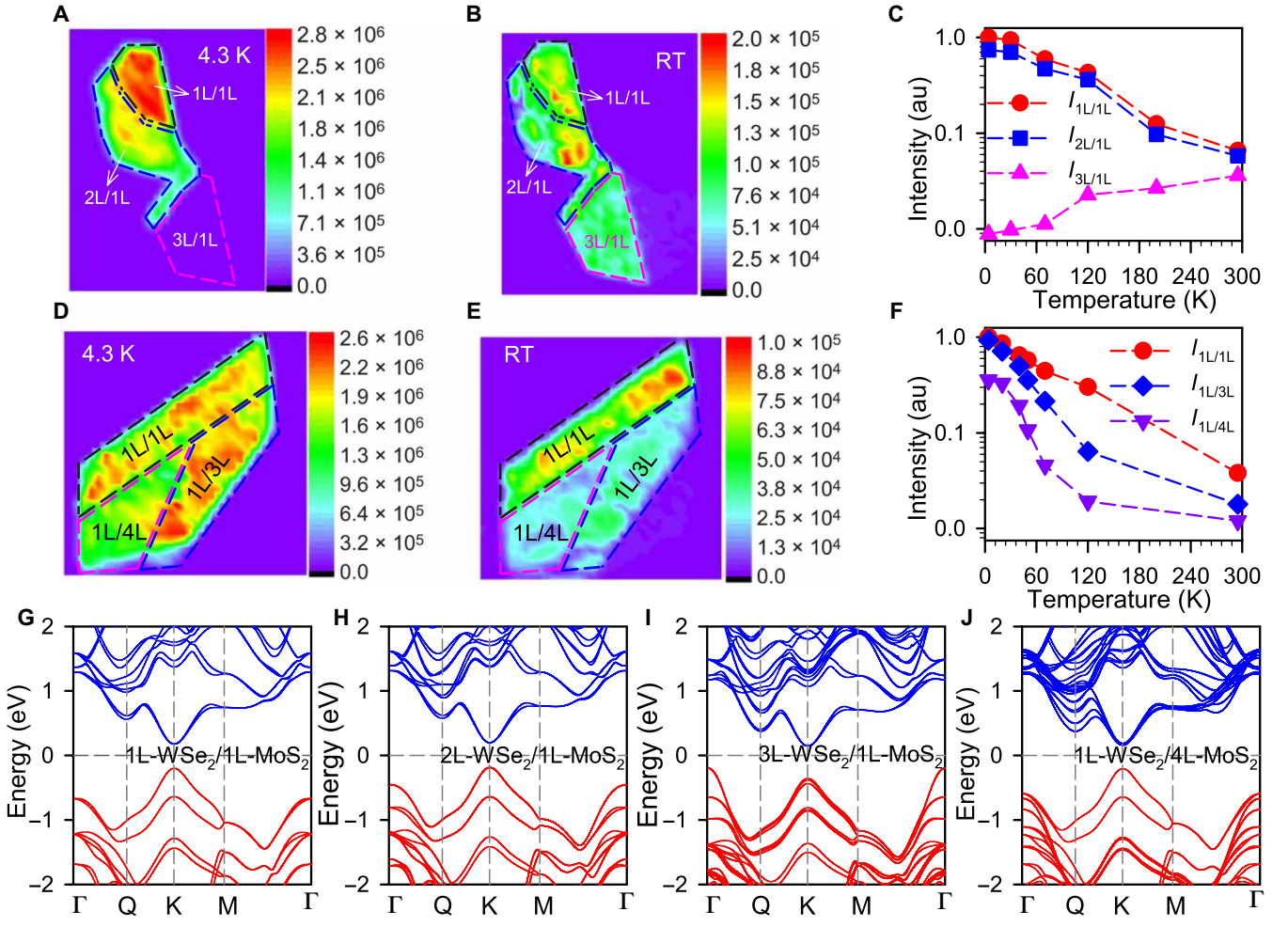

Fig. 2. Temperature dependence of IXs in mL-WSe_2/1L-MoS_2 and 1L-WSe_2/mL-MoS_2 heterostructures. (**A** and **B**) The PL intensity map of the IXs in mL-WSe_2/1L-MoS_2 (mL/1L; $m = 1$ to 3) HS at 4.3 K and room temperature, respectively. (**C**) The PL intensity of IXs in mL-WSe_2/1L-MoS_2 as a function of temperature. The PL intensity is the average values of multiple positions of each mL-WSe_2/1L-MoS_2 region. (**D** and **E**) The PL intensity map of the IXs in 1L-WSe_2/mL-MoS_2 (mL/1L; $m = 1$, 3, and 4) HS at 4.3 K and room temperature, respectively. A 1064-nm long pass was used to ensure that only the IX signal can be detected. (**F**) The PL intensity of IXs in 1L-WSe_2/mL-MoS_2 as a function of temperature. The PL intensity is the average values of multiple positions of each 1L-WSe_2/mL-MoS_2 region. (**G** to **J**) The calculated electronic energy structure of 1L-WSe_2/1L-MoS_2, 2L-WSe_2/1L-MoS_2, 3L-WSe_2/1L-MoS_2, and 1L-WSe_2/4L-MoS_2 heterostructures, respectively.

In contrast to the case in mL-WSe_2/1L-MoS_2 heterostructure, the IX PL intensity in 1L-WSe_2/mL-MoS_2 ($m = 1$, 3, and 4) heterostructure regions is strong at low temperature, and it decreases with increasing temperature (Fig. 2, D to F, and fig. S16). Similar behavior has been observed in other samples up to $m = 6$ (see section S5 and fig. S14). These results suggest that the 1L-WSe_2/mL-MoS_2 heterostructure is a direct bandgap semiconductor, and the bright state is the ground state, at least for MoS_2 up to four layers. To confirm these analyses, we calculate the band structures of the 1L-WSe_2/mL-MoS_2 heterostructure and mL-WSe_2/1L-MoS_2 heterostructure based on the density functional theory (DFT). These calculated results (see Fig. 2, G to J, and figs. S16 and S17) agree well with the experimental observations. Similar calculated results of 1L-WSe_2/1L-MoS_2 also show its direct bandgap nature (*8*, *34*), which is consistent with our results. On the other hand, we should note that the parameters and methods should be carefully chosen owing to its effects on the theory calculated results (*34*, *35*).

In addition, we also note that IX PL intensity in 2L-WSe_2/3L-MoS_2 heterostructure decreases with increasing temperature, indicating that it is a direct bandgap semiconductor (see section S5 and fig. S14). This result is in line with our analysis above that the conduction band minimum/CBM (valence band maximum/VBM) is mainly affected by MoS_2 (WSe_2) layers with both 3L-MoS_2 CBM and 2L-WSe_2 VBM located at K (K′) point, although both 2L-WSe_2 and 3L-MoS_2 are indirect bandgap semiconductor. Our DFT calculation further confirms the direct band of 2L-WSe_2/3L-MoS_2 heterostructure (see section S5 and fig. S19). These results open the door to design the direct bandgap heterostructure semiconductors for future optoelectronic device applications based on the layer engineering of multilayer TMDs. More results and discussion regarding the power dependence of the IX in 1L-WSe_2/mL-MoS_2 can be found in section S5 and fig. S20.

Valley polarization for IXs in multilayer heterostructures

Valley polarization has been used to probe the valley index in 2D TMDs. A natural question is as follows: How about the IX valley polarization in our multilayer heterostructures? With the optical selection rule (Fig. 3A), the valley is coupled with the PL circular

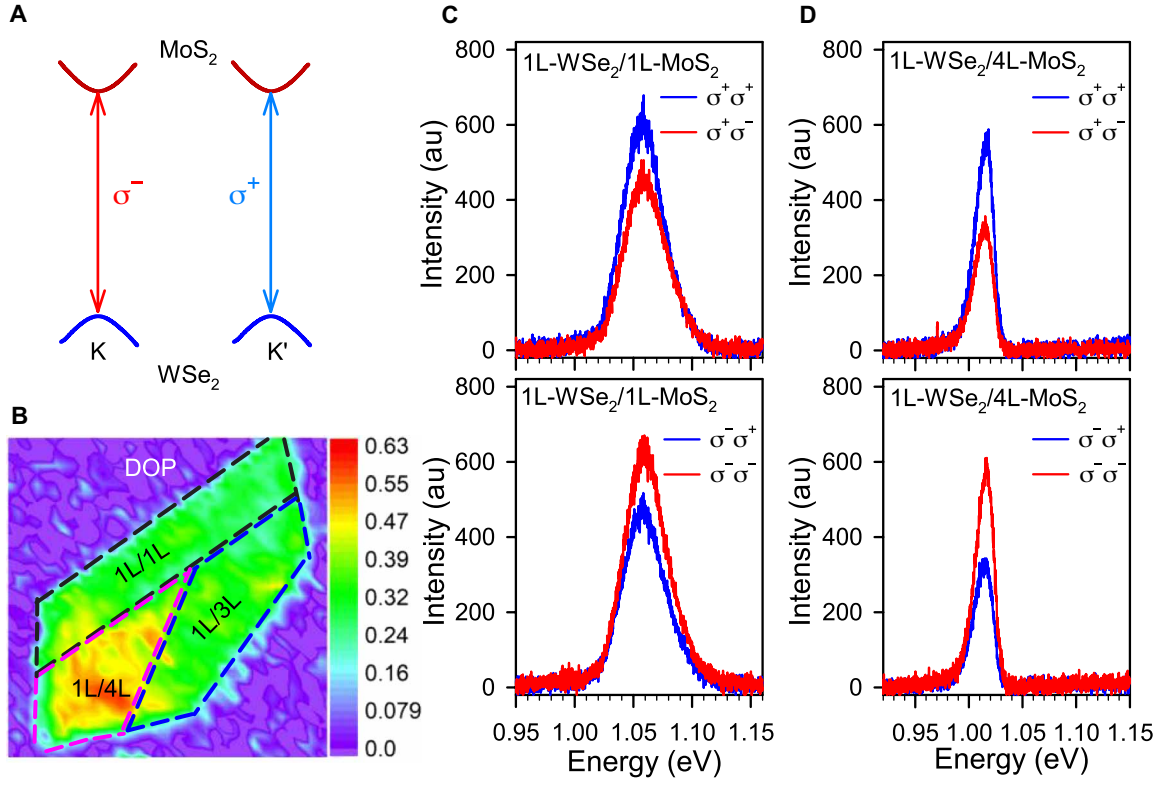

Fig. 3. Circularly polarized PL spectra of IXs in 1L-WSe_2/mL-MoS_2 heterostructures. (**A**) A simplified schematic of valley optical selection rule for IXs in K and K′ valley. The electrons and holes are located at K (K′) point of the MoS_2 conduction band and WSe_2 valence band, respectively. (**B**) The valley DOP mapping of IXs in the multilayer HS calculated from the polarized PL intensity mapping measurement results. (**C** and **D**) The circularly polarized PL spectra of IXs from 1L-WSe_2/1L-MoS_2 and 1L-WSe_2/4L-MoS_2 heterostructure regions, respectively. $\sigma^j\sigma^j$ represents excitation with σ^j and detection with σ^j circular polarization.

polarization, and therefore, we can characterize the valley properties through circular polarization–resolved PL measurement. Figure 3B shows the corresponding valley DOP mapping, and Fig. 3 (C and D) shows the corresponding circularly polarized PL spectra, respectively. Here, we define DOP $= \frac{I_{\sigma^-\sigma^-} - I_{\sigma^-\sigma^+}}{I_{\sigma^-\sigma^-} + I_{\sigma^-\sigma^+}}$, where $I_{\sigma^j\sigma^k}$ represents the PL intensity with σ^j excitation and σ^k detection, and $\sigma^+(\sigma^-)$denotes the right (left) circularly polarized light. As shown in Fig. 3B, all heterostructure regions show a high valley DOP. This indicates that the valley optical selection rule is valid in the 1L-WSe_2/mL-MoS_2 heterostructure, i.e., $\sigma^-(\sigma^+)$ IX emission coupled primarily to K (K′) valley. The observation also agrees with the recent report for the K-K transition nature for the IX emission in the infrared range for the monolayer-monolayer case (*8*, *26*). Similar results are obtained for other 1L-WSe_2/mL-MoS_2 samples (see section S6 and figs. S22 to S26). Moreover, The IX valley polarization of 1L-WSe_2/mL-MoS_2 heterostructure is quite robust and can persist up to room temperature, which is desired for valley device applications (see section S6 and fig. S24).

On the contrary, we find that the DOP for mL-WSe_2/1L-MoS_2 ($m > 1$) heterostructure is negligible (see section S6 and fig. S21). Upon resonant excitation with σ^- (σ^+) circularly polarized light (726 nm), the WSe_2 excitons are selectively created. Then, an ultrafast charge transfer process takes the electrons from the multilayer WSe_2 layers to the K (K′) valley of monolayer MoS_2 layer (*36*–*38*), leaving only the holes in the multilayer WSe_2 layers (*36*–*38*). Therefore, the vanishing valley polarization in the 2L-WSe_2/1L-MoS_2 case can only be attributed to the hole interlayer hopping between the WSe_2 layers. This can be further confirmed by calculating the charge density distribution of holes in WS_2 layers (see section S6 and fig. S21). In addition, in the 3L-WSe_2/1L-MoS_2 case, the VBM locates at Γ valley, which can couple equally to both polarizations. Consequently, the valley polarization of IX vanishes in mL-WSe_2/1L-MoS_2 ($m > 1$) and 2L-WSe_2/3L-MoS_2 heterostructures (see section S6 and fig. S25). This is in stark difference with 1L-WSe_2/mL-MoS_2 heterostructure. In the latter case, the VBM at the K (K′) valley is mainly contributed by 1L-WSe_2, where the orbital mixing of the VBM is largely suppressed. Meanwhile, the interlayer hopping for electrons between mL-MoS_2 layers vanishes at K points due to the symmetry of the d_{z^2} orbital (*33*). Hence, the valley optical selection rule of IXs in the 1L-WSe_2/1L-MoS_2 case is maintained for 1L-WSe_2/mL-MoS_2 heterostructures.

Enhanced valley lifetime for layer-engineered IXs at zero magnetic field

We found that IX in 1L-WSe_2/mL-MoS_2 ($m > 1$) heterostructure has a longer lifetime and valley lifetime than IX in 1L-WSe_2/1L-MoS_2 heterostructure. Figure 4 (A to C) shows the time-resolved circularly polarized PL of IXs from 1L-WSe_2/mL-MoS_2 heterostructure regions in Fig. 1D. For the copolarized emission (i.e., the collected emission polarization is the same as the excitation polarization), the data fit very well with a biexponential function. The slowest decay component

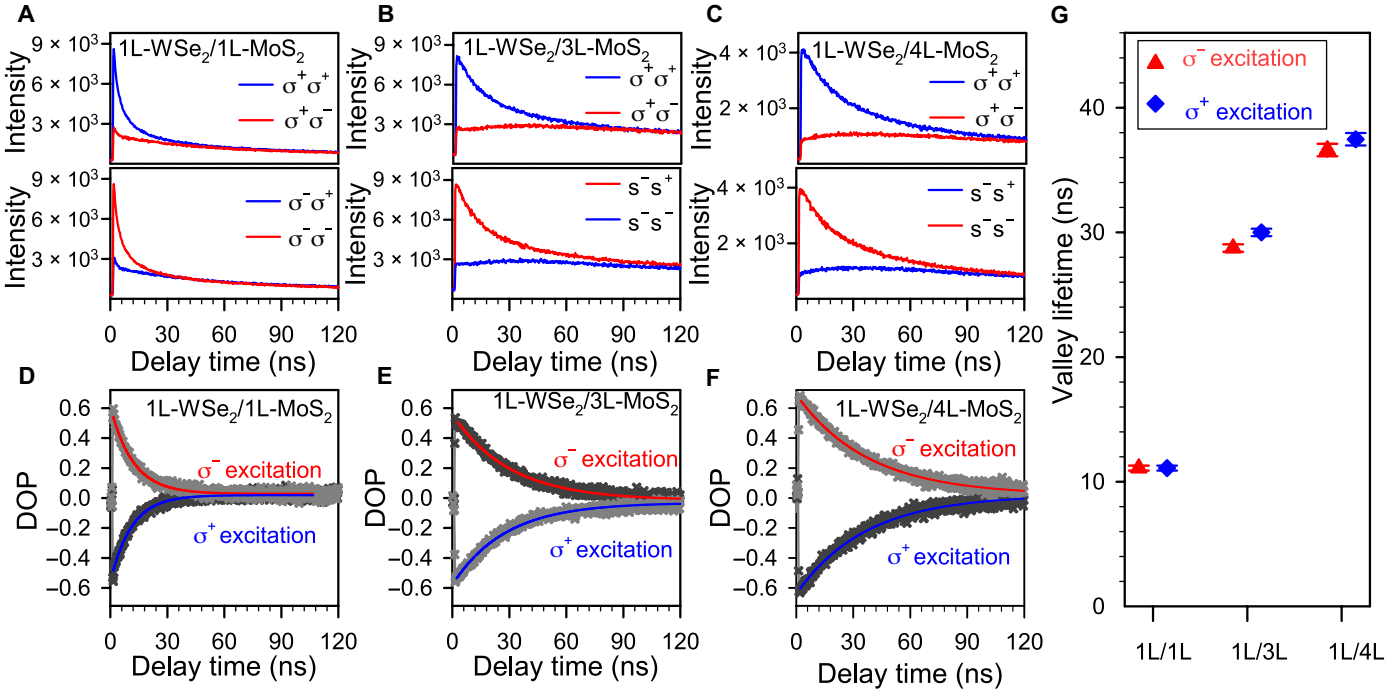

Fig. 4. Layer-engineered depolarization lifetime of IX in 1L-WSe_2/mL-MoS_2 heterostructures. (**A** to **C**) Time-resolved circularly polarized PL of IXs from 1L-WSe_2/1L-MoS_2, 1L-WSe_2/3L-MoS_2, and 1L-WSe_2/4L-MoS_2 HS regions, respectively. The IX lifetime of a few hundred nanoseconds was observed. The temperature for PL decay measurements is 4.3 K. (**D** to **F**) The time-resolved valley DOP of IXs obtained from the measured time-resolved circularly polarized PL in (A) to (C). (**G**) The valley DOP lifetimes under left and right circularly polarized light excitation.

is up to hundreds of nanoseconds, which is an order of magnitude longer than previously reported results for IX lifetimes (*7*, *17*, *39*). All decay components are slower in the 1L-WSe_2/3L-MoS_2 and 1L-WSe_2/4L-MoS_2 region as compared to the values in the 1L-WSe_2/1L-MoS_2 region. In contrast, the lifetime of IXs in mL-WSe_2/1L-MoS_2 heterostructure is decreased with more WSe_2 layers (section S7 and fig. S27). These results indicate that the number of MoS_2 layers can be used to increase the lifetime of IXs.

On the basis of the time-resolved PL data, we calculate the valley (DOP) lifetime. Figure 4 (D to F) shows the time-resolved DOP at 4.3 K. We fit the data with a single exponential decay function to obtain the valley lifetime. We find that the valley lifetime of IXs depends on the number of MoS_2 layers. The DOP decay shows a similar trend with the count decay, i.e., it is getting slower as the number of MoS_2 layers is increased. In particular, the valley lifetime increases from 11 ± 0.2 ns in the 1L-WSe_2/1L-MoS_2 region to 29 ± 0.3 ns in the 1L-WSe_2/3L-MoS_2 region and 37 ± 0.5 ns in the 1L-WSe_2/4L-MoS_2 region (Fig. 4G). We get similar results for different samples (section S7 and figs. S28 and S29). These results indicate that the valley lifetime has been increased by three to four times with the increasing number of MoS_2 layers.

The layer dependence of the IX lifetime and valley lifetime can be explained by considering that both exciton oscillator strength and electron-hole exchange interaction are suppressed in multilayer heterostructure when the wave function overlap between electron and hole is reduced (*16*). Similar to the case of multiple quantum well (*40*), the electron wave function spreads more as the number of MoS_2 layers is increased. As a result, the reduced electron-hole wave function overlap of IXs in 1L-WSe_2/mL-MoS_2 heterostructure leads to a longer exciton lifetime and valley lifetime. More results and discussion about the temperature dependence of the valley lifetime in 1L-WSe_2/mL-MoS_2 heterostructure can be found in section S8 and fig. S30.

Magnetic field enhanced valley polarization and valley lifetime

With applied magnetic field, we found that the valley polarization and valley lifetime can be further enhanced for IXs in 1L-WSe_2/mL-MoS_2. Figure 5A shows copolarized and cross-polarized PL spectra. One can clearly see the enlarged difference in spectrum between the two cases, representing an enhanced valley polarization. To examine the magnetic field dependence in more detail, we plot DOP under different magnetic fields, as shown in Fig. 5B. It shows that the amplitude of DOP has increased markedly from ~0.1 to 0.2 to ~0.7 to 0.8 by applying a tiny magnetic field. This is the case for all three situations of IXs in 1L-WSe_2/mL-MoS_2 (m = 1, 3, and 4). This implies that the origin of increased DOP is similar in these three cases. For IXs in 1L-WSe_2/4L-MoS_2, a prolonged valley lifetime has been shown in Fig. 5 (C and D) as well. Considering that we are exciting resonantly with the WSe_2 bright A exciton transition (726 nm), the magnetic field–induced increased DOP and prolonged valley lifetime can be attributed to the suppression of valley relaxation of WSe_2 excitons with magnetic fields. The suppression of the valley mixing by small perpendicular magnetic field has been discussed in some reports (*15*, *41*). For the IX, the increased DOP and valley lifetime of IX emission are attributed to the suppression of Maialle-Silva-Sham–like intervalley scattering (*13*) of the long-lived intralayer exciton before it decays to become an IX (*15*). More magnetic field–dependent

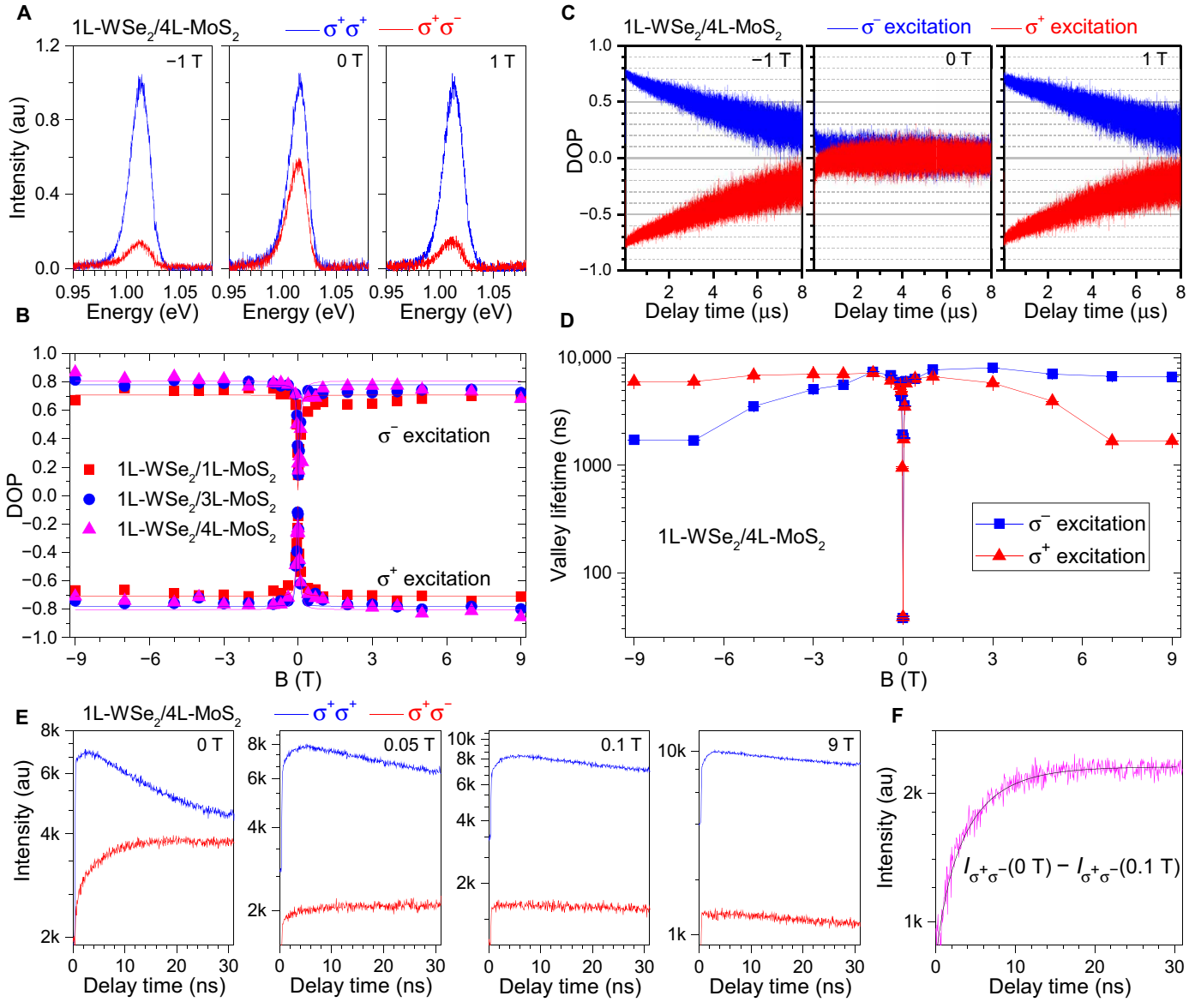

Fig. 5. Suppression of valley relaxation under magnetic field for IXs in 1L-WSe_2/mL-MoS_2 heterostructures. (**A**) Valley polarization for IXs in 1L-WSe_2/4L-MoS_2 under three magnetic fields: −1, 0, and 1 T. An enhanced valley polarization under magnetic field has been observed. (**B**) Magnetic dependence of DOP. Valley mixing has been suppressed for all $m = 1$, 3, and 4 cases. (**C**) Time-resolved DOP for IXs in 1L-WSe_2/4L-MoS_2 at −1, 0, and 1 T (0.125-MHz repetition rate is used here). An enhanced valley polarization lifetime has been observed under magnetic field. (**D**) The magnetic field dependence of valley DOP lifetime under left and right circularly polarized light excitation, respectively. (**E**) Time-resolved photon emission at different magnetic fields. (**F**) The magnetic field suppressed valley relaxation characterization. The temperature for all measurements under magnetic fields is around 4.3 K.

results of IXs in 1L-WSe_2/mL-MoS_2 are presented in section S9 and figs. S31 to S33.

It is worth noting that the valley relaxation is slow in 1L-WSe_2/4L-MoS_2 such that the valley mixing time constant is comparable with the PL decay lifetime. This leads to the fact that the cross-polarized PL count shows an initial count increase, rather than an exponential decay, as shown in Fig. 5E. To extract the information for this valley mixing mechanism, we ramp up the magnetic field. One can clearly see the suppression of the cross-polarized PL counts with the increase of magnetic field, which comes from the suppression of valley mixing. One can give an estimation of the valley mixing time constant of 5 ± 1 ns in this case, by fitting the cross-polarized PL count at 0 T or simply subtracting the count rate in the magnetic field from the zero-field case (Fig. 5F). We should note that this valley mixing time scale is much slower than that in monolayer TMDs (*42*). Our result represents the first direct observation of valley mixing in the time domain from PL emission, thanks to the prolonged exciton lifetimes in multilayer heterostructure.

In summary, we studied the IXs from multilayer WSe_2/MoS_2 heterostructures. We demonstrated that the layer number of WSe_2 and MoS_2 offers an additional degree of freedom to modulate the emission spectra, as well as enhancing the exciton lifetime, valley

polarization, and valley lifetime of IXs. The 1L-WSe_2/mL-MoS_2 heterostructure preserves the direct bandgap at least for MoS_2 up to four layers. These results demonstrate that novel phenomena can be achieved by layer engineering of multilayer 2D semiconductor materials, which offers a systematic approach readily extended to other 2D materials. While we did not use a deterministic layer engineering method in our report, recent advances in 2D material fabrication method allows this method (*43*). This deterministic layer engineering method combined with the twist angle manipulation in vdW heterostructure will bring many opportunities for fundamental research and optoelectronic device applications.

MATERIALS AND METHODS

Sample fabrication

1L-MoS_2 and mL-MoS_2 and 1L-WSe_2 and mL-WSe_2 are first exfoliated mechanically from bulk crystals on PDMS stamps. The alignment between MoS_2 and WSe_2 layers is done by first choosing these samples that have two sharp edges with a 120° angle. We then used the dry transfer method to stack MoS_2 and WSe_2 samples by aligning the edge of the top and bottom samples onto an ultralow doping Si substrate that is covered by 285 nm of SiO_2 to form the WSe_2/MoS_2 and hBN/WSe_2/MoS_2/hBN heterostructures at room temperature. Last, the heterostructure samples were annealed under ultrahigh vacuum (around 10 to 6 mbar) at 200°C for 3 hours.

Optical measurements

PL measurement

A homemade confocal microscope is used to perform the polarization and spatially resolved PL spectroscopy. The polarization state of the excitation and the detection are controlled by a combination of polarizers, half-wave plates, and quarter-wave plates installed on the excitation and detection. The PL spectra were obtained by a spectrometer (Andor Shamrock) with a charge-coupled device (CCD) detector. Unless otherwise stated, a laser with 726 nm was used as the excitation source at low temperatures. A 50× objective lens with a spot size of 1 μm [numerical aperture (NA) = 0.65] is used to collect the signal. The sample temperature is controlled using a cryostat (Montana Instruments and Attocube, Attodry 1000). For pulse experiments, a 726-nm diode laser (full width at half maximum of <80 ps, maximum repetition rate is 80 MHz) is used for exciting the sample. The intensity map is obtained by detecting the emission using a superconducting single-photon detector while scanning the excitation position on the sample by using a galvo system. If not otherwise stated, the continuous wave (CW) laser power for the PL measurement at low temperatures is around 100 μW. For PL decay measurements, the CW-equivalent laser power for pulse laser is around 0.25 μW.

Raman measurement

The Raman spectra were measured at room temperature with the T64000 Raman system, equipped with a liquid nitrogen–cooled CCD. A 100× objective lens (NA = 0.95) is used to collect the signal. The excitation wavelength for Raman spectra measurement is 532 nm. The laser power for Raman measurements is around 200 μW.

SHG measurements

The SHG measurements are performed at room temperature. A pulse laser from a Ti:Sapphire oscillator (Spectra Physics, Tsunami) with a peak at around 870 nm, a repetition rate of 80 MHz, and a pulse duration of 100 fs was used as the excitation source. The laser power is around 0.6 mW.

Theoretical calculations

We performed first-principles calculations using the Vienna ab initio simulation package (*44*) with the projector augmented wave method (*45*). The Perdew-Burke-Ernzerhof type (*46*) generalized gradient approximation was used for the exchange-correlation functional. The heterostructures were constructed by taking the average of the experimental lattice constant of bulk materials [the lattice constant for MoS_2 is $a = b = 3.168$ Å (*47*) and for WSe_2 is $a = b = 3.282$ Å (*48*)]. We set the interlayer distance to 6.67 Å between MoS_2 and WSe_2 initially and then relax the interlayer distance and atomic coordinates. The cutoff energy was set to 500 eV, and a $16 \times 16 \times 1$ Γ-centered k-point mesh was used for the Brillouin zone sampling. The convergence criteria for the energy and force were set to 10^{-5} eV and 0.01 eV/Å, respectively. A vacuum layer with a thickness of 20 Å was taken to avoid artificial interactions between periodic images. The vdW corrections were taken into account by the approach of Dion *et al.* (*49*). To get a more accurate energy gap, we also used the more sophisticated Heyd-Scuseria-Ernzerhof hybrid functional method (HSE06) for the exchange-correlation potential (*50*) to calculate the band structure for the 1L/1L heterostructure.

SUPPLEMENTARY MATERIALS

Supplementary material for this article is available at http://advances.sciencemag.org/cgi/content/full/7/30/eabh0863/DC1

REFERENCES AND NOTES

1. G. Wang, A. Chernikov, M. M. Glazov, T. F. Heinz, X. Marie, T. Amand, B. Urbaszek, *Colloquium*: Excitons in atomically thin transition metal dichalcogenides. *Rev. Mod. Phys.* **90**, 021001 (2018).
2. A. Splendiani, L. Sun, Y. Zhang, T. Li, J. Kim, C.-Y. Chim, G. Galli, F. Wang, Emerging photoluminescence in monolayer MoS_2. *Nano Lett.* **10**, 1271–1275 (2010).
3. K. F. Mak, C. Lee, J. Hone, J. Shan, T. F. Heinz, Atomically thin MoS_2: A new direct-gap semiconductor. *Phys. Rev. Lett.* **105**, 136805 (2010).
4. E. M. T. Fadaly, A. Dijkstra, J. R. Suckert, D. Ziss, M. A. J. van Tilburg, C. Mao, Y. Ren, V. T. van Lange, K. Korzun, S. Kölling, M. A. Verheijen, D. Busse, C. Rödl, J. Furthmüller, F. Bechstedt, J. Stangl, J. J. Finley, S. Botti, J. E. M. Haverkort, E. P. A. M. Bakkers, Direct-bandgap emission from hexagonal Ge and SiGe alloys. *Nature* **580**, 205–209 (2020).
5. W. Zhao, Z. Ghorannevis, L. Chu, M. Toh, C. Kloc, P.-H. Tan, G. Eda, Evolution of electronic structure in atomically thin sheets of WS_2 and WSe_2. *ACS Nano* **7**, 791–797 (2013).
6. A. K. Geim, I. V. Grigorieva, Van der Waals heterostructures. *Nature* **499**, 419–425 (2013).
7. P. Rivera, J. R. Schaibley, A. M. Jones, J. S. Ross, S. Wu, G. Aivazian, P. Klement, K. Seyler, G. Clark, N. J. Ghimire, J. Yan, D. G. Mandrus, W. Yao, X. Xu, Observation of long-lived interlayer excitons in monolayer $MoSe_2$–WSe_2 heterostructures. *Nat. Commun.* **6**, 6242 (2015).
8. O. Karni, E. Barré, S. C. Lau, R. Gillen, E. Y. Ma, B. Kim, K. Watanabe, T. Taniguchi, J. Maultzsch, K. Barmak, R. H. Page, T. F. Heinz, Infrared interlayer exciton emission in MoS_2/WSe_2 heterostructures. *Phys. Rev. Lett.* **123**, 247402 (2019).
9. P. Rivera, H. Yu, K. L. Seyler, N. P. Wilson, W. Yao, X. Xu, Interlayer valley excitons in heterobilayers of transition metal dichalcogenides. *Nat. Nanotechnol.* **13**, 1004–1015 (2018).
10. J. R. Schaibley, H. Yu, G. Clark, P. Rivera, J. S. Ross, K. L. Seyler, W. Yao, X. Xu, Valleytronics in 2D materials. *Nat. Rev. Mater.* **1**, 16055 (2016).
11. Z. Gong, G.-B. Liu, H. Yu, D. Xiao, X. Cui, X. Xu, W. Yao, Magnetoelectric effects and valley-controlled spin quantum gates in transition metal dichalcogenide bilayers. *Nat. Commun.* **4**, 2053 (2013).
12. H. Zeng, J. Dai, W. Yao, D. Xiao, X. Cui, Valley polarization in MoS_2 monolayers by optical pumping. *Nat. Nanotechnol.* **7**, 490–493 (2012).
13. T. Yu, M. W. Wu, Valley depolarization due to intervalley and intravalley electron-hole exchange interactions in monolayer MoS_2. *Phys. Rev. B* **89**, 205303 (2014).
14. M. M. Glazov, T. Amand, X. Marie, D. Lagarde, L. Bouet, B. Urbaszek, Exciton fine structure and spin decoherence in monolayers of transition metal dichalcogenides. *Phys. Rev. B* **89**, 201302 (2014).
15. C. Jiang, W. Xu, A. Rasmita, Z. Huang, K. Li, Q. Xiong, W.-b. Gao, Microsecond dark-exciton valley polarization memory in two-dimensional heterostructures. *Nat. Commun.* **9**, 753 (2018).

16. J. Kim, C. Jin, B. Chen, H. Cai, T. Zhao, P. Lee, S. Kahn, K. Watanabe, T. Taniguchi, S. Tongay, M. F. Crommie, F. Wang, Observation of ultralong valley lifetime in WSe_2/MoS_2 heterostructures. *Sci. Adv.* **3**, e1700518 (2017).
17. P. Rivera, K. L. Seyler, H. Yu, J. R. Schaibley, J. Yan, D. G. Mandrus, W. Yao, X. Xu, Valley-polarized exciton dynamics in a 2D semiconductor heterostructure. *Science* **351**, 688–691 (2016).
18. Z. Wang, D. A. Rhodes, K. Watanabe, T. Taniguchi, J. C. Hone, J. Shan, K. F. Mak, Evidence of high-temperature exciton condensation in two-dimensional atomic double layers. *Nature* **574**, 76–80 (2019).
19. K. L. Seyler, P. Rivera, H. Yu, N. P. Wilson, E. L. Ray, D. G. Mandrus, J. Yan, W. Yao, X. Xu, Signatures of moiré-trapped valley excitons in $MoSe_2/WSe_2$ heterobilayers. *Nature* **567**, 66–70 (2019).
20. B. Zhu, H. Zeng, J. Dai, Z. Gong, X. Cui, Anomalously robust valley polarization and valley coherence in bilayer WS_2. *Proc. Natl. Acad. Sci. U.S.A.* **111**, 11606–11611 (2014).
21. C. Jin, J. Kim, M. I. B. Utama, E. C. Regan, H. Kleemann, H. Cai, Y. Shen, M. J. Shinner, A. Sengupta, K. Watanabe, T. Taniguchi, S. Tongay, A. Zettl, F. Wang, Imaging of pure spin-valley diffusion current in WS_2-WSe_2 heterostructures. *Science* **360**, 893–896 (2018).
22. Y.-M. Li, J. Li, L.-K. Shi, D. Zhang, W. Yang, K. Chang, Light-induced exciton spin Hall effect in van der Waals heterostructures. *Phys. Rev. Lett.* **115**, 166804 (2015).
23. H. Heo, J. H. Sung, S. Cha, B.-G. Jang, J.-Y. Kim, G. Jin, D. Lee, J.-H. Ahn, M.-J. Lee, J. H. Shim, H. Choi, M.-H. Jo, Interlayer orientation-dependent light absorption and emission in monolayer semiconductor stacks. *Nat. Commun.* **6**, 7372 (2015).
24. G. Hu, Q. Ou, G. Si, Y. Wu, J. Wu, Z. Dai, A. Krasnok, Y. Mazor, Q. Zhang, Q. Bao, C.-W. Qiu, A. Alù, Topological polaritons and photonic magic angles in twisted α-MoO_3 bilayers. *Nature* **582**, 209–213 (2020).
25. E. M. Alexeev, D. A. Ruiz-Tijerina, M. Danovich, M. J. Hamer, D. J. Terry, P. K. Nayak, S. Ahn, S. Pak, J. Lee, J. I. Sohn, M. R. Molas, M. Koperski, K. Watanabe, T. Taniguchi, K. S. Novoselov, R. V. Gorbachev, H. S. Shin, V. I. Fal'ko, A. I. Tartakovskii, Resonantly hybridized excitons in moiré superlattices in van der Waals heterostructures. *Nature* **567**, 81–86 (2019).
26. Y. Liu, H. Fang, A. Rasmita, Y. Zhou, J. Li, T. Yu, Q. Xiong, N. Zheludev, J. Liu, W. Gao, Room temperature nanocavity laser with interlayer excitons in 2D heterostructures. *Sci. Adv.* **5**, eaav4506 (2019).
27. K. Tran, G. Moody, F. Wu, X. Lu, J. Choi, K. Kim, A. Rai, D. A. Sanchez, J. Quan, A. Singh, J. Embley, A. Zepeda, M. Campbell, T. Autry, T. Taniguchi, K. Watanabe, N. Lu, S. K. Banerjee, K. L. Silverman, S. Kim, E. Tutuc, L. Yang, A. H. MacDonald, X. Li, Evidence for moiré excitons in van der Waals heterostructures. *Nature* **567**, 71–75 (2019).
28. K. S. Thygesen, Calculating excitons, plasmons, and quasiparticles in 2D materials and van der Waals heterostructures. *2D Materials* **4**, 022004 (2017).
29. H.-P. Komsa, A. V. Krasheninnikov, Effects of confinement and environment on the electronic structure and exciton binding energy of MoS2 from first principles. *Phys. Rev. B* **86**, 241201 (2012).
30. L. Li, W. Zheng, C. Ma, H. Zhao, F. Jiang, Y. Ouyang, B. Zheng, X. Fu, P. Fan, M. Zheng, Y. Li, Y. Xiao, W. Cao, Y. Jiang, X. Zhu, X. Zhuang, A. Pan, Wavelength-tunable interlayer exciton emission at the near-infrared region in van der Waals semiconductor heterostructures. *Nano Lett.* **20**, 3361–3368 (2020).
31. X.-X. Zhang, Y. You, S. Y. F. Zhao, T. F. Heinz, Experimental evidence for dark excitons in monolayer WSe_2. *Phys. Rev. Lett.* **115**, 257403 (2015).
32. S. Tongay, J. Zhou, C. Ataca, K. Lo, T. S. Matthews, J. Li, J. C. Grossman, J. Wu, Thermally driven crossover from indirect toward direct bandgap in 2D semiconductors: $MoSe_2$ versus MoS_2. *Nano Lett.* **12**, 5576–5580 (2012).
33. P. V. Nguyen, N. C. Teutsch, N. P. Wilson, J. Kahn, X. Xia, A. J. Graham, V. Kandyba, A. Giampietri, A. Barinov, G. C. Constantinescu, N. Yeung, N. D. M. Hine, X. Xu, D. H. Cobden, N. R. Wilson, Visualizing electrostatic gating effects in two-dimensional heterostructures. *Nature* **572**, 220–223 (2019).
34. S. Latini, K. T. Winther, T. Olsen, K. S. Thygesen, Interlayer excitons and band alignment in MoS_2/hBN/WSe_2 van der Waals heterostructures. *Nano Lett.* **17**, 938–945 (2017).
35. F. Bussolotti, H. Kawai, Z. E. Ooi, V. Chellappan, D. Thian, A. L. C. Pang, K. E. J. Goh, Roadmap on finding chiral valleys: Screening 2D materials for valleytronics. *Nano Futures* **2**, 032001 (2018).
36. X. Hong, J. Kim, S.-F. Shi, Y. Zhang, C. Jin, Y. Sun, S. Tongay, J. Wu, Y. Zhang, F. Wang, Ultrafast charge transfer in atomically thin MoS_2/WS_2 heterostructures. *Nat. Nanotechnol.* **9**, 682–686 (2014).
37. C. Jin, E. Y. Ma, O. Karni, E. C. Regan, F. Wang, T. F. Heinz, Ultrafast dynamics in van der Waals heterostructures. *Nat. Nanotechnol.* **13**, 994–1003 (2018).
38. W. Xu, W. Liu, J. F. Schmidt, W. Zhao, X. Lu, T. Raab, C. Diederichs, W. Gao, D. V. Seletskiy, Q. Xiong, Correlated fluorescence blinking in two-dimensional semiconductor heterostructures. *Nature* **541**, 62–67 (2017).
39. Z. Huang, Y. Liu, K. Dini, Q. Tan, Z. Liu, H. Fang, J. Liu, T. Liew, W. Gao, Robust room temperature valley Hall effect of interlayer excitons. *Nano Lett.* **20**, 1345–1351 (2020).
40. H. V. Demir, S. V. Gaponenko, *Applied Nanophotonics Chapter 2* (Cambridge Univ. Press, 2018).
41. T. Smoleński, M. Goryca, M. Koperski, C. Faugeras, T. Kazimierczuk, A. Bogucki, K. Nogajewski, P. Kossacki, M. Potemski, Tuning valley polarization in a WSe_2 monolayer with a tiny magnetic field. *Phys. Rev. X* **6**, 021024 (2016).
42. Z. Wang, A. Molina-Sánchez, P. Altmann, D. Sangalli, D. De Fazio, G. Soavi, U. Sassi, F. Bottegoni, F. Ciccacci, M. Finazzi, L. Wirtz, A. C. Ferrari, A. Marini, G. Cerullo, S. Dal Conte, Intravalley spin–flip relaxation dynamics in single-layer WS_2. *Nano Lett.* **18**, 6882–6891 (2018).
43. F. Liu, W. Wu, Y. Bai, S. H. Chae, Q. Li, J. Wang, J. Hone, X.-Y. Zhu, Disassembling 2D van der Waals crystals into macroscopic monolayers and reassembling into artificial lattices. *Science* **367**, 903–906 (2020).
44. G. Kresse, J. Hafner, Ab initio molecular-dynamics simulation of the liquid-metal–amorphous-semiconductor transition in germanium. *Phys. Rev. B* **49**, 14251–14269 (1994).
45. P. E. Blöchl, Projector augmented-wave method. *Phys. Rev. B* **50**, 17953–17979 (1994).
46. J. P. Perdew, K. Burke, M. Ernzerhof, Generalized gradient approximation made simple. *Phys. Rev. Lett.* **77**, 3865–3868 (1996).
47. V. Petkov, S. J. L. Billinge, P. Larson, S. D. Mahanti, T. Vogt, K. K. Rangan, M. G. Kanatzidis, Structure of nanocrystalline materials using atomic pair distribution function analysis: Study of $LiMoS_2$. *Phys. Rev. B* **65**, 092105 (2002).
48. W. J. Schutte, J. L. De Boer, F. Jellinek, Crystal structures of tungsten disulfide and diselenide. *J. Solid State Chem.* **70**, 207–209 (1987).
49. M. Dion, H. Rydberg, E. Schröder, D. C. Langreth, B. I. Lundqvist, Van der Waals density functional for general geometries. *Phys. Rev. Lett.* **92**, 246401 (2004).
50. J. Heyd, G. E. Scuseria, M. Ernzerhof, Hybrid functionals based on a screened Coulomb potential. *J. Solid State Chem.* **118**, 8207–8215 (2003).
51. X. Zhang, X.-F. Qiao, W. Shi, J.-B. Wu, D.-S. Jiang, P.-H. Tan, Phonon and Raman scattering of two-dimensional transition metal dichalcogenides from monolayer, multilayer to bulk material. *Chem. Soc. Rev.* **44**, 2757–2785 (2015).
52. X. Luo, Y. Zhao, J. Zhang, M. Toh, C. Kloc, Q. Xiong, S. Y. Quek, Effects of lower symmetry and dimensionality on Raman spectra in two-dimensional WSe_2. *Phys. Rev. B* **88**, 195313 (2013).
53. L. Liang, J. Zhang, B. G. Sumpter, Q.-H. Tan, P.-H. Tan, V. Meunier, Low-frequency shear and layer-breathing modes in Raman scattering of two-dimensional materials. *ACS Nano* **11**, 11777–11802 (2017).
54. J.-B. Wu, H. Wang, X.-L. Li, H. Peng, P.-H. Tan, Raman spectroscopic characterization of stacking configuration and interlayer coupling of twisted multilayer graphene grown by chemical vapor deposition. *Carbon* **110**, 225–231 (2016).
55. N. R. Wilson, P. V. Nguyen, K. Seyler, P. Rivera, A. J. Marsden, Z. P. L. Laker, G. C. Constantinescu, V. Kandyba, A. Barinov, N. D. M. Hine, X. Xu, D. H. Cobden, Determination of band offsets, hybridization, and exciton binding in 2D semiconductor heterostructures. *Sci. Adv.* **3**, e1601832 (2017).
56. P. Nagler, G. Plechinger, M. V. Ballottin, A. Mitioglu, S. Meier, N. Paradiso, C. Strunk, A. Chernikov, P. C. M. Christianen, C. Schüller, T. Korn, Interlayer exciton dynamics in a dichalcogenide monolayer heterostructure. *2D Materials* **4**, 025112 (2017).
57. A. Ciarrocchi, D. Unuchek, A. Avsar, K. Watanabe, T. Taniguchi, A. Kis, Polarization switching and electrical control of interlayer excitons in two-dimensional van der Waals heterostructures. *Nat. Photonics* **13**, 131–136 (2019).
58. C. Jiang, A. Rasmita, W. Xu, A. Imamoğlu, Q. Xiong, W.-B. Gao, Optical spin pumping induced pseudomagnetic field in two-dimensional heterostructures. *Phys. Rev. B* **98**, 241410 (2018).
59. W. Li, X. Lu, S. Dubey, L. Devenica, A. Srivastava, Dipolar interactions between localized interlayer excitons in van der Waals heterostructures. *Nat. Mater.* **19**, 624–629 (2020).
60. B. Laikhtman, R. Rapaport, Exciton correlations in coupled quantum wells and their luminescence blue shift. *Phys. Rev. B* **80**, 195313 (2009).

Acknowledgments

Funding: We acknowledge the financial support from the Singapore National Research Foundation through its Competitive Research Program (CRP award nos. NRF-CRP21-2018-0007, NRF-CRP22-2019-0004, and NRF-CRP23-2019-0002), Singapore Ministry of Education [MOE2016-T2-1-163 and MOE2016-T3-1-006 (S)], A*Star QTE programme. **Author contributions:** Q.T. prepared the samples. Q.T., Z.H., and S. Liu carried out the measurements. S. Li and S.A.Y. performed the theoretical calculations. Q.T., A.R., Q.X., K.S.N., and W.-b.G. analyzed the experimental data. All authors contributed to writing the manuscript. Q.T., S.A.Y., K.S.N., and W.-b.G. conceived and supervised the project. **Competing interests:** The authors declare that they have no competing interests. **Data and materials availability:** All data needed to evaluate the conclusions in the paper are present in the paper and/or the Supplementary Materials. Additional data related to this paper may be requested from the authors.

Submitted 15 February 2021
Accepted 7 June 2021
Published 23 July 2021
10.1126/sciadv.abh0863

Citation: Q. Tan, A. Rasmita, S. Li, S. Liu, Z. Huang, Q. Xiong, S. A. Yang, K. S. Novoselov, W.-b. Gao, Layer-engineered interlayer excitons. *Sci. Adv.* **7**, eabh0863 (2021).